



Improving Wind Turbine Drivetrain Reliability Using a Combined Experimental, Computational, and Analytical Approach

Y. Guo and J. van Dam
National Renewable Energy Laboratory

R. Bergua and J. Jové
ALSTOM Wind S.L.U.

J. Campbell
ALSTOM Wind

*Presented at the ASME 2014 International Design Engineering Technical Conferences & Computers and Information in Engineering Conference (IDETC/CIE 2014)
Buffalo, New York
August 17–20, 2014*

**NREL is a national laboratory of the U.S. Department of Energy
Office of Energy Efficiency & Renewable Energy
Operated by the Alliance for Sustainable Energy, LLC**

This report is available at no cost from the National Renewable Energy Laboratory (NREL) at www.nrel.gov/publications.

Conference Paper
NREL/CP-5000-61683
March 2015

Contract No. DE-AC36-08GO28308

NOTICE

The submitted manuscript has been offered by an employee of the Alliance for Sustainable Energy, LLC (Alliance), a contractor of the US Government under Contract No. DE-AC36-08GO28308. Accordingly, the US Government and Alliance retain a nonexclusive royalty-free license to publish or reproduce the published form of this contribution, or allow others to do so, for US Government purposes.

This report was prepared as an account of work sponsored by an agency of the United States government. Neither the United States government nor any agency thereof, nor any of their employees, makes any warranty, express or implied, or assumes any legal liability or responsibility for the accuracy, completeness, or usefulness of any information, apparatus, product, or process disclosed, or represents that its use would not infringe privately owned rights. Reference herein to any specific commercial product, process, or service by trade name, trademark, manufacturer, or otherwise does not necessarily constitute or imply its endorsement, recommendation, or favoring by the United States government or any agency thereof. The views and opinions of authors expressed herein do not necessarily state or reflect those of the United States government or any agency thereof.

This report is available at no cost from the National Renewable Energy Laboratory (NREL) at www.nrel.gov/publications.

Available electronically at <http://www.osti.gov/scitech>

Available for a processing fee to U.S. Department of Energy and its contractors, in paper, from:

U.S. Department of Energy
Office of Scientific and Technical Information
P.O. Box 62
Oak Ridge, TN 37831-0062
phone: 865.576.8401
fax: 865.576.5728
email: <mailto:reports@adonis.osti.gov>

Available for sale to the public, in paper, from:

U.S. Department of Commerce
National Technical Information Service
5285 Port Royal Road
Springfield, VA 22161
phone: 800.553.6847
fax: 703.605.6900
email: orders@ntis.fedworld.gov
online ordering: <http://www.ntis.gov/help/ordermethods.aspx>

Cover Photos: (left to right) photo by Pat Corkery, NREL 16416, photo from SunEdison, NREL 17423, photo by Pat Corkery, NREL 16560, photo by Dennis Schroeder, NREL 17613, photo by Dean Armstrong, NREL 17436, photo by Pat Corkery, NREL 17721.

IMPROVING WIND TURBINE DRIVETRAIN RELIABILITY USING A COMBINED EXPERIMENTAL, COMPUTATIONAL, AND ANALYTICAL APPROACH

Yi Guo^{1,*}, Roger Bergua², Jeroen van Dam¹, Jordi Jove², and Jon Campbell³

¹ National Renewable Energy Laboratory
15013 Denver West Parkway
Golden, Colorado 80401, USA

² ALSTOM Wind S.L.U.
Roc Boronat, 78
08005 Barcelona, Spain

³ ALSTOM Wind
1100 Boulders Pkwy
Richmond, VA 23225, USA

ABSTRACT

Nontorque loads induced by the wind turbine rotor overhang weight and aerodynamic forces can greatly affect drivetrain loads and responses. If not addressed properly, these loads can result in a decrease in gearbox component life. This work uses analytical modeling, computational modeling, and experimental data to evaluate a unique drivetrain design that minimizes the effects of nontorque loads on gearbox reliability: the Pure Torque® drivetrain developed by Alstom. The drivetrain has a hub-support configuration that transmits nontorque loads directly into the tower rather than through the gearbox as in other design approaches. An analytical model of Alstom's Pure Torque drivetrain provides insight into the relationships among turbine component weights, aerodynamic forces, and the resulting drivetrain loads. Main shaft bending loads are orders of magnitude lower than the rated torque and are hardly affected by wind conditions and turbine operations.

1 INTRODUCTION

Premature gearbox failures in wind turbines have a significant impact on the cost of wind farm operations [1]. Geared drivetrains, the most prevalent design for land-based wind turbines, consist of a main shaft, main bearing(s), gearbox, generator coupling, and generator. Different rotor supports and bearing configurations are used by manufacturers and can be grouped into four categories: 1) three-point suspension, 2) two-main-bearing suspension, 3) integrated suspension, and 4) torque only suspension, such as Alstom's Pure Torque drivetrain. In the three-point suspension, the rear main bearing of the two main shaft bearings is integrated into the gearbox at the planetary stage as the planetary carrier bearing. The two-main-bearing suspension uses two separate

main bearings that ideally transmit all the nontorque loads from the rotor into the tower through the bedplate. The integrated drivetrain has the main bearings integrated into the gearbox. The nontorque loads are transmitted through the gearbox housing. The torque only drivetrain is distinct from the others as it uses a set of flexible couplings to connect the rotor with the main shaft thus isolating most nontorque loads from the drivetrain, including the rotor overhang weight. Of these drivetrain configurations, the three-point suspension drivetrain, historically the most widely used configuration, is the most sensitive to nontorque loads.

Horizontal-axis wind turbine drivetrains carry various combinations of torque and nontorque loads. Nontorque loads are primarily caused by the rotor overhang weight and aerodynamic loads. Tests conducted by the National Renewable Energy Laboratory (NREL) Gearbox Reliability Collaborative (GRC) on a three-point suspension drivetrain showed that it transmits significant main shaft bending loads into the gearbox [2][3]. The main shaft pitching moments measured in the dynamometer and field tests are 29% to 64% of rated input torque [3].

Nontorque loads are one of the major sources of gearbox reliability issues that contribute to premature gearbox failures or internal component damage [4][2][5][6]. Nontorque loads affected the planetary load sharing, gear load distribution, and bearing load at the planetary gear stage of the GRC gearbox [7]. Planetary gears use a number of nearly or equally-spaced planet gears that share the loads. However, planet gear loads are rarely equally-shared among the planets [8][9]. The planetary load sharing factor is the ratio between the maximum torque that a single planet gear carries and the average torque among all planet gears. The degree of unequal load sharing has

* Corresponding author. National Renewable Energy Laboratory, 15013 Denver West Parkway, Golden, CO 80401-3305. Tel: +1-303-384-7187, Fax: +1-303-384-6901, Email address: yi.guo@nrel.gov (Yi Guo)

implications of tolerance schemes and gearbox loads. All of these parameters affect the design and fatigue life of the planet gears and bearings.

Different combinations of torque and nontorque loads can cause gear edge load, tooth pitting, bearing fatigue, and skidding. Gear tooth edge loading was observed during the GRC experiments. The edge loading was caused by unequal planet bearing loads between upwind and downwind rows and by misalignment [10] caused by nontorque loads. Micropitting induced by the edge contact was evident on the upwind side of the ring gear teeth. Planet bearings may become pitted during the high torque events such as those experienced during some braking events. Nontorque loads and manufacturing tolerances cause cyclic planet bearing forces around the rotor rotation frequency and its higher harmonics. The combination of the cyclic bearing loading and the initial pits that occur during high torque events can cause bearing pitting over time. At low torque, the planet bearings are susceptible to skidding, which compromises the desired pure rolling condition of the bearing and reduces bearing life. The sensitivity to nontorque loads is an inherent reliability issue of three-point suspension drivetrains.

The major objective of this study was to evaluate the Alstom drivetrain solutions for minimizing the impacts of nontorque loads using modeling and experimental approaches. The approaches included the field testing, a high-fidelity computational model established in SAMCEF [11], and a reduced-order analytical model. Field testing of the Alstom ECO100 turbine was conducted at the National Wind Technology Center (NWTC) at NREL, and extensive data on turbine and drivetrain loads were collected. Experimental data were correlated with the modeling results and they helped justify the modeling assumptions and boundaries. The computational model included all wind turbine components, which accounted for the interaction between the drivetrain and the rest of the turbine. The analytical formulation provided insight on the load-path of the nontorque loads between the rotor and the drivetrain.

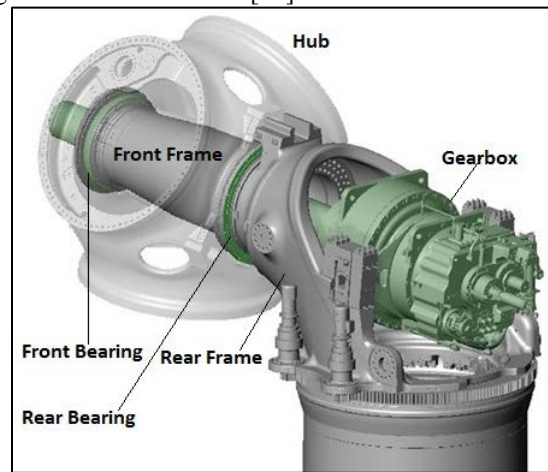
2 A DRIVETRAIN DESIGN SOLUTION TO ELIMINATE NONTORQUE LOADS

2.1 Drivetrain Configuration

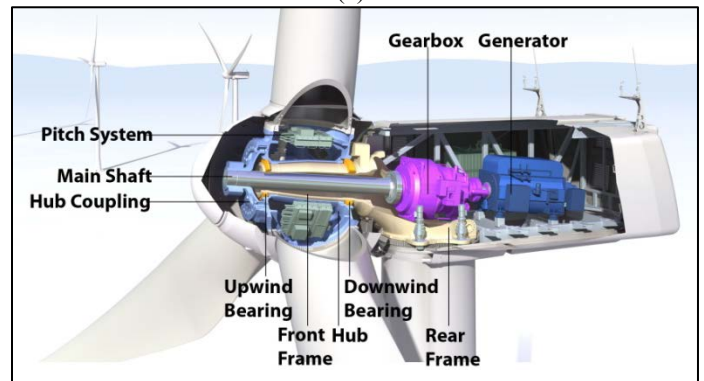
This study analyzed Alstom’s ECO100 wind turbine with a power rating of 3 MW. Alstom is addressing the aforementioned drivetrain reliability issues by utilizing a unique hub support configuration. The Pure Torque design prevents most rotor nontorque loads from entering the drivetrain. The hub support configuration is illustrated in Figure 1(a). An extended bedplate beneath the hub, called the front frame, is used to transfer rotor nontorque loads to the tower. A spread pair of tapered roller bearings is mounted on the front frame to support the rotor. The rotor center of gravity is in the middle of the two main bearings. This configuration minimizes the moment between main bearings caused by the rotor weight.

The main bearings react to the aerodynamic loads. A set of flexible couplings are mounted circumferentially on the front face elastically connecting the main shaft to the hub, as shown in Figure 1(b). The couplings layout is designed to provide flexibility in axial, radial, and tilting directions, effectively interrupting the nontorque load path from the hub to the shaft while providing a relatively high rotational stiffness for transmitting the torque to the shaft. The flexible couplings account for dynamic misalignments during operation and static misalignments caused by assembly tolerances. The gearbox sits on elastomer trunnions that provide rigidity in the vertical and rotational directions and add flexibility in the horizontal and tilting directions.

The geared drivetrain includes a low-speed shaft, shrink disk, three-stage gearbox, mechanical brake, generator coupling, and generator. The gearbox has two planetary stages and a helical gear pair. The first two gearbox stages have four and three planet gears, respectively. General turbine configuration is discussed in [12].



(a)



(b)

Figure 1. (a) Alstom’s Pure Torque drivetrain (b) hub support

2.2 Study Approaches

This study used multiple approaches to evaluate Alstom’s Pure Torque drivetrain, including field testing of Alstom’s ECO100 wind turbine at the NWTC, a computational turbine model, and an analytical model. The experimental

results were used to verify the established models. The computational model of the turbine was established in SAMCEF, which includes the blades, hub, bedplate, tower, foundation, and drivetrain. The analytical model is static and is useful for providing insight on the nontorque load path.



Figure 2. ECO100 3 MW Wind turbine at the NWTC

2.2.1 Field Testing

Alstom’s test turbine is located at NREL’s NWTC, at an altitude of approximately 1,840 m above sea level with an air density close to 1 kg/m^3 . Figure 2 shows the test turbine with a meteorological tower in the background that measures wind speed, wind shear, wind direction, air temperature, and air pressure. The test site has a relatively high turbulence intensity level as shown in Figure 3. All three of the turbine’s blades were instrumented to measure the blade root bending moments in the flap and lead-lag directions. Two bending bridges were installed near the middle of the front frame to measure the bending moments. Strain gauges were also mounted at the tower base to measure the side-side bending, fore-aft bending, and torque. The main shaft was instrumented for torque and bending in two perpendicular directions. The measurement plane was located at 25% of the main shaft length upwind from the gearbox. Proximity sensors were mounted at the gearbox torque arms to measure the horizontal displacement and torsional misalignment. Measurements were collected under the following load cases: normal production, emergency stop, parked or idling, normal start up, and shut down.

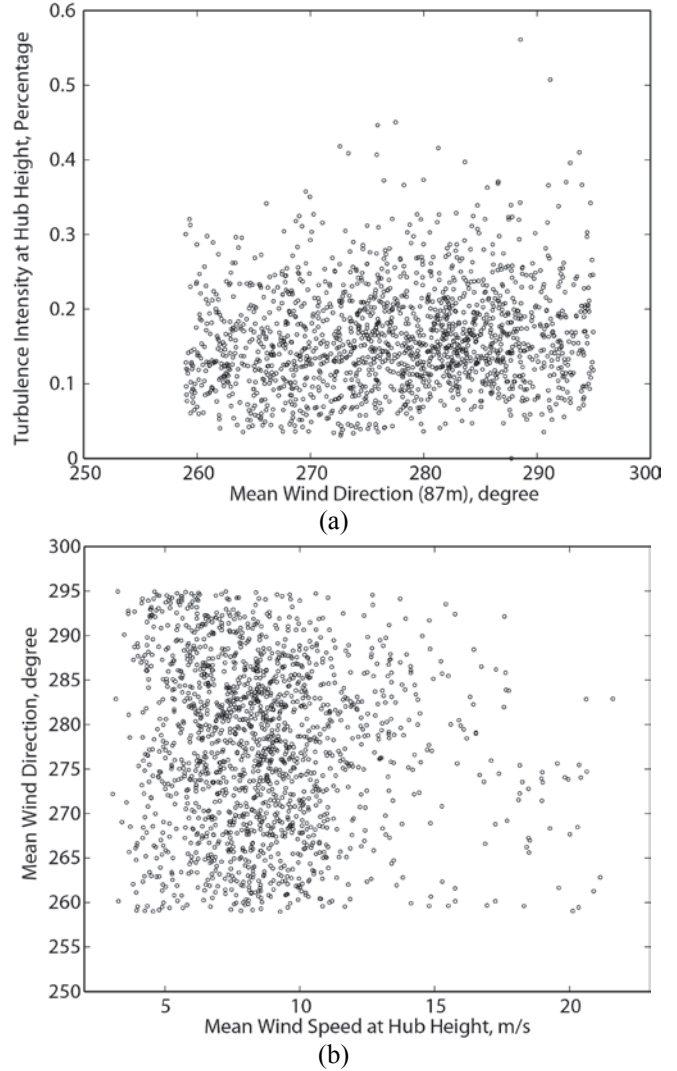


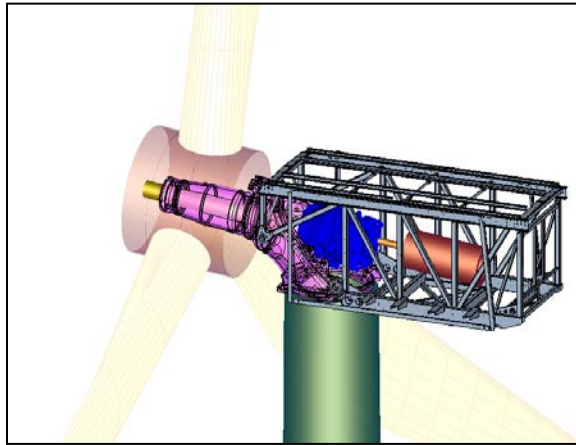
Figure 3. (a) turbulence intensity and (b) wind direction average at Site 4.1 at the NWTC

2.2.2 Computational Model

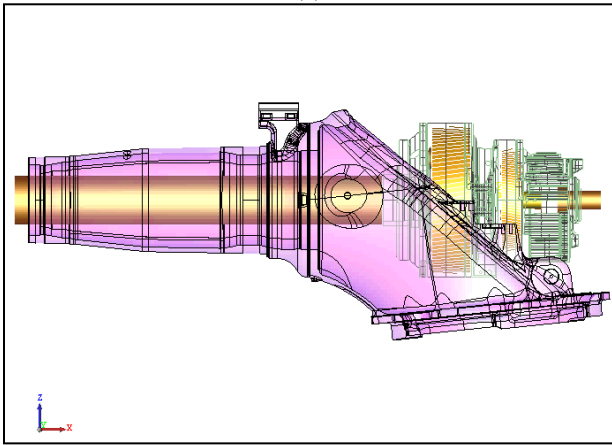
The ECO100 wind turbine was modeled in SAMCEF Wind Turbine version 3.2 as shown in Figure 4(a). SAMCEF incorporates an implicit nonlinear dynamic finite element approach with multibody system functionalities. SAMCEF iteratively solves the nonlinear equations of the system’s motion. Further details on the integration procedure, error estimators, and solution strategies can be found in [11]. Unlike FAST [14] and GH BLADED [13], SAMCEF includes a detailed gearbox model and structural flexibilities of the drivetrain. These advantages make it suitable to study the effects of nontorque loads on drivetrain dynamic responses.

The wind turbine model includes blades, hub, frames, main shaft, gearbox, tower, and foundation with more than 3,000 degrees of freedom. The flexibilities of key structural components were accounted for by using a combination of nonlinear beams and super elements. The blades, tower, and main shaft were modeled using nonlinear Timoshenko beams

that account for extension, bending, shear, and torsion. The front, main and rear frames (shown in Figure 5(a)), gearbox housing, and planetary carriers were modeled initially by finite element models. The Craig-Bampton condensation technique [15] was then applied to reduce the degrees of freedom of these finite element models and improve the computational efficiency. Only nodes (super elements) at crucial locations were retained. These locations included the interfaces between the frame and the hub coupling, main bearings, gearbox trunnions, generator mounts, and the yaw drive.



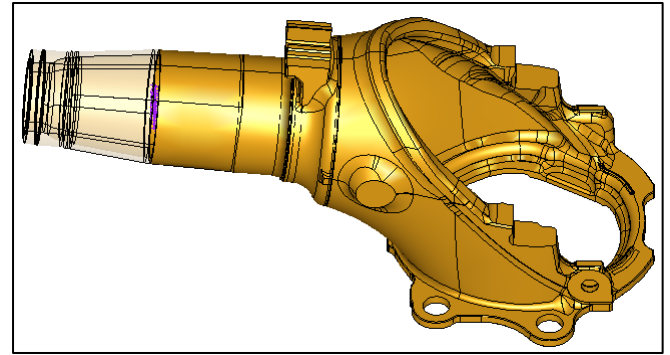
(a)



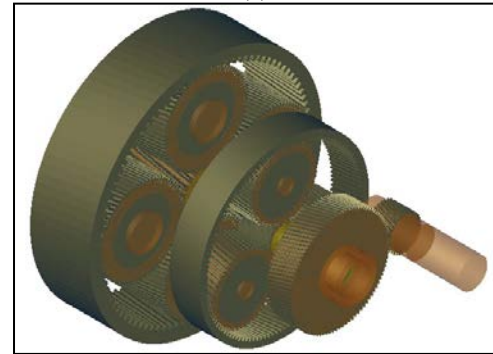
(b)

Figure 4. The computational models established in SAMCEF: (a) the turbine, (b) drivetrain

The drivetrain module, shown in Figure 4(b), included the flexible front and main frames, main shaft, main bearings, gearbox, gearbox trunnions, generator coupling, and generator. Each gear was modeled as an element with six degrees of freedom. The gear model considered helix angle, pressure angle, module, backlash, number of teeth, and gear tooth loads as shown in Figure 5(b). Gear microgeometry and mesh stiffness variation were not considered. Bearings are modeled by nonlinear stiffness functions with clearances in radial and axial directions. Only diagonal terms in the stiffness matrices of the bearings were considered.



(a)



(b)

Figure 5. (a) front frame and (b) gearbox models in SAMCEF

Aerodynamic loads were calculated based on the blade element momentum theory (BEM) with wind turbine specific corrections for tip and hub losses, wake effects, tower shadow effect, dynamic inflow, and dynamic stall [16][17][18]. TurbSim [19] generated the turbulent wind fields used in this study with wind shear and profiles defined by the IEC standard [20] but adjusted to the test site conditions for density and turbulence intensity. Turbulent wind loads were simulated to statistically compare turbine response/loads against experiments at various cut-in and cut-out wind speeds. Steady wind was used to simulate transient events (i.e. emergency stop). Gravity forces of individual components of the turbine were also included.

2.2.3 Analytical Model

The analytical model described the transfer path of nontorque loads and calculated the drivetrain loads in Alstom's Pure Torque drivetrain. The results were used with the experimental and computational modeling approaches to evaluate the Pure Torque design drivetrain. The main shaft force diagram is shown in Figure 6. The nomenclature is shown in Table 1.

Table 1. Nomenclature for the analytical model

| | |
|--------------------------------|---|
| L_1 | Distance between the hub coupling and upwind main bearing |
| L_2 | Distance between the hub coupling and downwind main bearing |
| L_{as} | Distance between the hub coupling and center of gravity of the main shaft |
| L_c | Distance between the hub coupling and center of gravity of the carrier |
| L_{cu} | Distance between the hub coupling and upwind carrier bearing |
| L_{cd} | Distance between the planet bearing and downwind carrier bearing |
| L_{FF} | Distance between the upwind main bearing and center of gravity of the front frame |
| L_{hb} | Distance between the hub coupling and hub center |
| L_{ms} | Main shaft length |
| L_{PL} | Distance between the hub coupling and planet bearing locations |
| L_s | Distance between the upwind main bearing and front frame sensor |
| k_{cu}^r, k_{cd}^r | Radial stiffnesses of the upwind and downwind carrier bearings |
| k_{cu}^t, k_{cd}^t | Tilting stiffnesses of the upwind and downwind carrier bearings |
| k_{B1}^r, k_{B2}^r | Radial stiffnesses of the upwind and downwind main bearings |
| k_{B1}^t, k_{B2}^t | Tilting stiffnesses of the upwind and downwind main bearings |
| W_c | Weight of the carrier |
| W_{FF} | Weight of the front frame |
| W_{hc} | Weight of the hub coupling |
| W_{ms} | Weight of the main shaft |
| W_{hb} | Weight of the hub and blade system |
| $F_{B1}^j, M_{B1}^j, j = y, z$ | Forces and moments at the upwind main bearing |
| $F_{B2}^j, M_{B2}^j, j = y, z$ | Forces and moments at the downwind main bearing |
| $F_{cu}^j, M_{cu}^j, j = y, z$ | Forces and moments at the upwind carrier bearing |
| $F_{cd}^j, M_{cd}^j, j = y, z$ | Forces and moments at the downwind carrier bearing |

| | |
|--------------------------------|---|
| $M_{hb}^j, j = y, z$ | Bending moments caused by aerodynamic forces and rotor weight at the hub center |
| $F_{hc}^j, M_{hc}^j, j = y, z$ | Forces and moments at the hub coupling |
| $F_{PL}^j, M_{PL}^j, j = y, z$ | Forces and moments at the geometric center of the planet bearings |
| $F_s^j, M_s^j, j = y, z$ | Forces and moments at the front frame sensor |
| $M_{sh}^j, j = y, z$ | Bending moments along the main shaft |

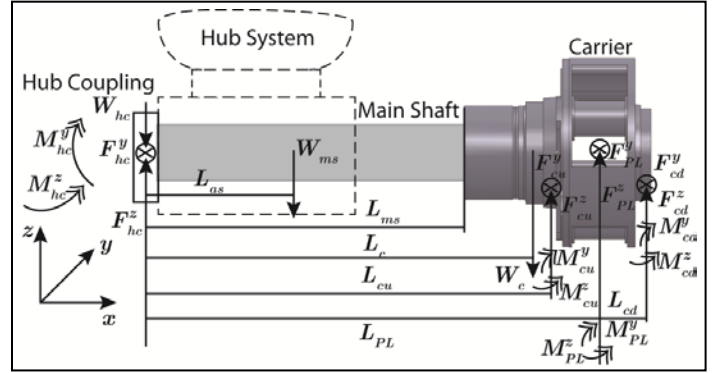


Figure 6. Force diagram of the main shaft

The following equations are derived based on the force and moment balance of the system.

The force balance along the horizontal axis $\sum F^y = 0$ leads to

$$F_{hc}^y + F_{cu}^y + F_{PL}^y + F_{cd}^y = 0 \quad (1)$$

The force balance along the vertical axis $\sum F^z = 0$ leads to

$$F_{hc}^z - W_{ms} - W_c - W_{hc} + F_{cu}^z + F_{PL}^z + F_{cd}^z = 0 \quad (2)$$

The balance of pitching moments $\sum M^y = 0$ around planet bearing locations leads to

$$M_{hc}^y + F_{hc}^z L_{PL} - W_{hc} L_{PL} - W_{ms} (L_{PL} - L_{as}) - W_c (L_{PL} - L_c) + F_{cu}^z (L_{PL} - L_{cu}) + M_{cu}^y + M_{PL}^y - F_{cd}^z L_{cd} + M_{cd}^y = 0 \quad (3)$$

The balance of yaw moments $\sum M^z = 0$ around planet bearing locations results in

$$M_{hc}^z - F_{hc}^y L_{PL} - F_{cu}^y (L_{PL} - L_{cu}) + M_{cu}^z + M_{PL}^z + F_{cd}^y L_{cd} + M_{cd}^z = 0 \quad (4)$$

The following assumptions are made based on system stiffness properties:

- Hub coupling moments are negligible because tilting stiffnesses of the hub coupling are significantly lower than main bearings, thus

$$M_{hc}^y, M_{hc}^z = 0 \quad (5)$$

- ii. Rotor loads in the y direction are transferred to the frame through the main bearings instead of the drivetrain through the hub coupling because the hub coupling stiffness is orders of magnitude smaller than main bearings.

$$F_{hc}^y = 0 \quad (6)$$

- iii. Drivetrain weight (main shaft and carrier) is supported by radial stiffnesses of the carrier bearings instead of bending stiffness because $k_{cu}^r L_{cu}^2 \gg k_{cu}^t, k_{cd}^t$ and $k_{cd}^r L_{cd}^2 \gg k_{cu}^t, k_{cd}^t$

$$M_{cu}^y = M_{cu}^z = M_{cd}^y = M_{cd}^z = 0 \quad (7)$$

- iv. Carrier bearings have high stiffnesses and smaller clearances than gear backlash, thus loads (mainly main shaft and carrier weight) are supported by carrier bearings and nearly only torque is transmitted to gear meshes. Furthermore, planet bearings are mounted in symmetry without positioning errors and unequal clearances. As a result, planet gears have equal load sharing, resulting in

$$F_{pl}^y = F_{pl}^z = 0 \quad (8)$$

$$M_{pl}^y = M_{pl}^z = 0 \quad (9)$$

A kinematic constraint is also applied to solve the undetermined system, as follows:

- v. The upwind carrier bearing is heavily loaded compared to the downwind bearing. Given the comparable load capacities of upwind and downwind carrier bearings, the distance between the hub or main shaft and the upwind carrier bearing is smaller than that with the downwind bearing, i.e.

$$F_{cu}^j \gg F_{cd}^j, j = y, z \quad (10)$$

This assumption could vary with different carrier bearing configurations used in different turbines. A sensitivity study on the effects of upwind and downwind carrier bearing stiffnesses on drivetrain loads is recommended to improve the calculation accuracy of the main shaft load.

The solutions of Eq. (1) - Eq. (4) are

$$\begin{cases} F_{hc}^z = \frac{W_{ms}(L_{cu} - L_{as}) + W_c(L_{cu} - L_c)}{L_{cu}} + W_{hc} \\ F_{cu}^z = W_{ms} \frac{L_{as}}{L_{cu}} + W_c \frac{L_c}{L_{cu}} \end{cases} \quad (11)$$

The main shaft bending moments along the main shaft are

$$\begin{cases} M_{sh}^y(x) = \left[\frac{W_{ms}(L_{cu} - L_{as}) + W_c(L_{cu} - L_c)}{L_{cu}} \right] x - \frac{1}{2} \frac{W_{ms}}{L_{ms}} x^2 \\ M_{sh}^z(x) = 0 \end{cases} \quad (12)$$

$x < L_{ms}$

As shown in equations (11) and (12), hub coupling and main shaft loads are only a function of the drivetrain weight. Although these equations are not general and cannot be used directly for another drivetrain design, this methodology can be applied to any drivetrain configuration to quantify the influence of nontorque loads on drivetrain loads. Using a similar approach, the forces and moments of the front frame and main bearings can also be formulated.

The force diagram of the hub and blades is shown in Figure 7(a) and Figure 7(b). Assumptions made for the hub and blades include

1. The hub moments are reacted by radial stiffnesses of main bearings because of

$$k_{B1}^t, k_{B2}^t \ll k_{B1}^r (L_{hb} - L_1)^2, k_{B2}^r (L_2 - L_{hb})^2, \text{ such that } M_{B1}^j, M_{B2}^j \ll M_{hb}^j, j = y, z \quad (13)$$

2. Aerodynamic radial and axial forces acting on the hub center and axial forces are not considered.

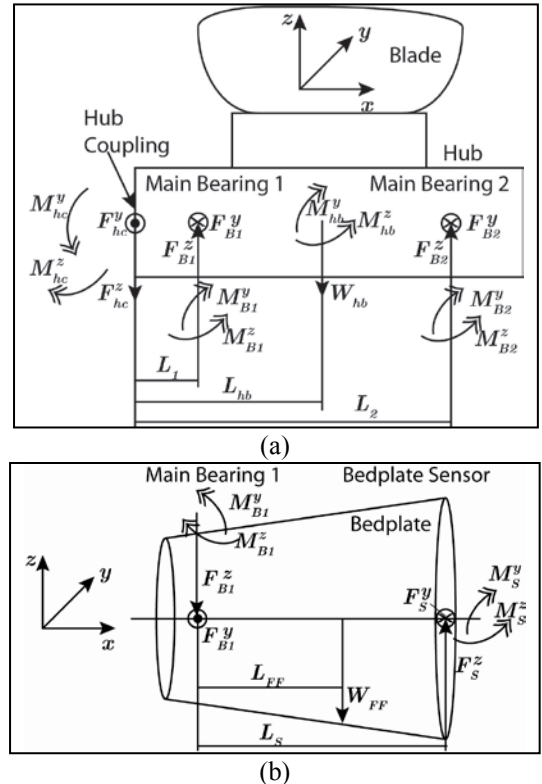


Figure 7. Force diagram of (a) the hub system and (b) front frame

The final form of the analytical solution is

$$\begin{aligned}
 F_{hc}^z &= \frac{W_{ms}(L_{cu} - L_{as}) + W_c(L_{cu} - L_c)}{L_{cu}} \\
 F_{cu}^z &= W_{ms} \frac{L_{as}}{L_{cu}} + W_c \frac{L_c}{L_{cu}} \\
 F_{cu}^y &= 0 \\
 F_{B1}^y &= \frac{M_{hb}^z}{L_2 - L_1} \\
 F_{B2}^y &= -\frac{M_{hb}^z}{L_2 - L_1} \\
 F_{B1}^z &= \frac{W_{hb}(L_2 - L_{hb}) - M_{hb}^y}{L_2 - L_1} + \frac{L_2}{L_{cu}(L_2 - L_1)} [W_{ms}(L_{cu} - L_{as}) + W_c(L_{cu} - L_c)] \\
 F_{B2}^z &= \frac{W_{hb}(L_{hb} - L_1) + M_{hb}^y}{L_2 - L_1} - \frac{L_1}{L_{cu}(L_2 - L_1)} [W_{ms}(L_{cu} - L_{as}) + W_c(L_{cu} - L_c)] \\
 M_s^y &= -\frac{L_s}{L_2 - L_1} M_{hb}^y + \frac{L_s L_2}{L_{cu}(L_2 - L_1)} [W_{ms}(L_{cu} - L_{as}) + W_c(L_{cu} - L_c)] \\
 &\quad + \frac{L_s}{L_2 - L_1} (L_2 - L_{hb}) W_{hb} + (L_s - L_{FF}) W_{FF} \\
 M_s^z &= -\frac{L_s}{L_2 - L_1} M_{hb}^z
 \end{aligned} \tag{14}$$

As shown in Eq. (14), the bedplate bending moments, M_s and main bearing loads, F_{B1} and F_{B2} , highly depend on the rotor loads. The weights of the rotor, front frame, and main shaft affect the bedplate bending moment about the y axis and main bearing loads in the z direction. Hub coupling loads (F_{hc}) are independent from aerodynamic loads and rotor weight being mainly driven by main shaft weight.

2.3 Main Shaft Bending Moment Sensitivity to Carrier's Center of Gravity and Loads

Sensitivity studies were performed to investigate the effects of the carrier's center of gravity (COG) and load sharing between upwind and downwind carrier bearings on main shaft bending moments as shown in Figure 8 and Figure 9. The results were calculated using the analytical model. As shown in Figure 8, the main shaft bending moment, M_y , increased or decreased when the carrier's COG was located upwind or downwind of the carrier geometric center. Therefore, the main shaft bending moment could be further reduced by artificially placing the carrier COG downwind. Furthermore, the load share between the upwind and downwind carrier bearings significantly affected the main shaft bending moment as shown in Figure 9. When the downwind carrier bearing carried all the loads, the maximum shaft bending moment increased more than 300% at the measurement point (shaft length of 0.75) compared to the case when the upwind bearing carries the loads. This suggests that using a higher stiffness for the upwind carrier

bearing than the downwind bearing can reduce the main shaft bending moment significantly.

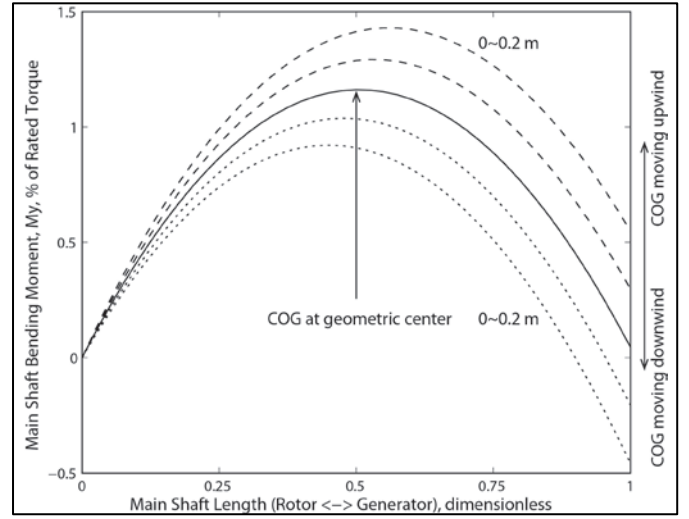


Figure 8. Main shaft bending moment, M_y , along the shaft when the carrier COG is located at the upwind and downwind of the geometric center

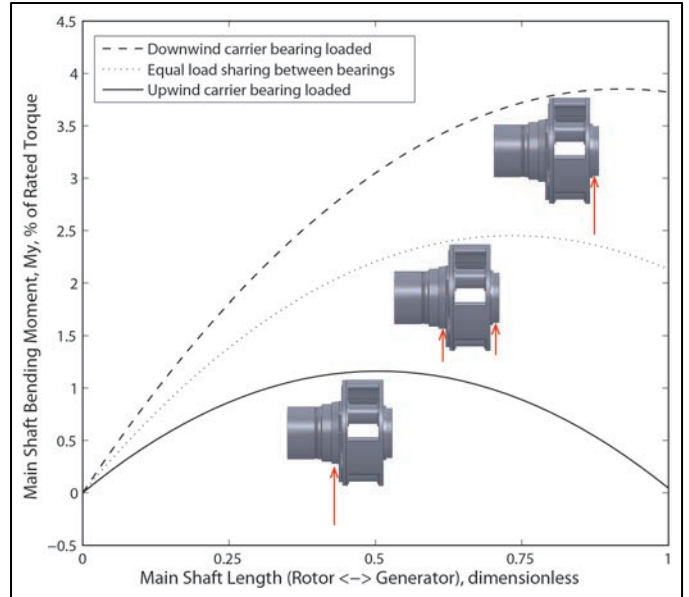


Figure 9. Main shaft bending moment, M_y , along the shaft when the carrier bearing loads are shared between two carrier bearings or carried by a single bearing

2.4 Model Validation by Experiment

Results calculated by the developed models were compared against experimental data collected during power production and transients. The comparison results included natural frequencies, blade loads, main shaft loads, and tower base loads.

2.4.1 Natural Frequency

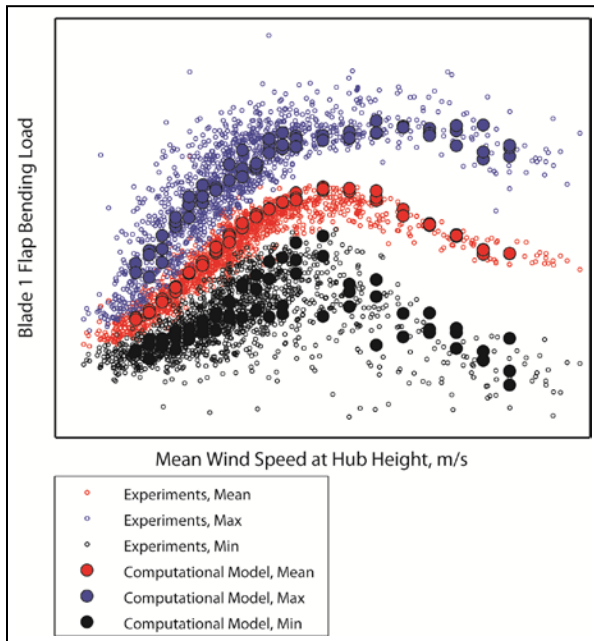
Wind turbine natural frequencies within the range from 0Hz to 2Hz were compared between the computational model and the experiment as shown in Table 2. Good agreement is evident, particularly with the first tower bending mode.

Table 2. Natural frequencies and modes of the ECO100 turbine

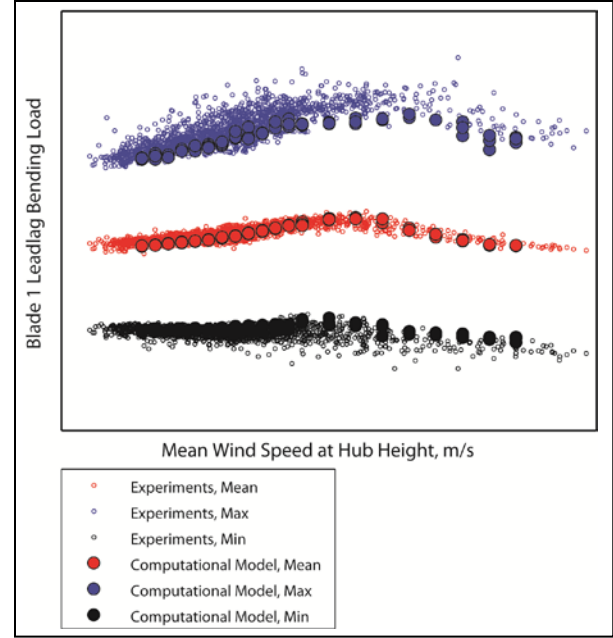
| Mode Shape | Frequency Difference % |
|---|------------------------|
| 1 st tower bending | 0.0 |
| 2 nd tower bending | -2.3 |
| 1 st blade flap (collective) | -2.8 |
| 1 st blade lead-lag (collective) | -5.3 |
| 1 st rotational drivetrain | +1.2 |

2.4.2 Turbine Loads during Power Production

Figure 10(a) and Figure 10(b) compare the modeling and experimental results of blade 1 flap and blade 1 lead-lag loads within the cut-in to cut-out wind speed range. The maximum, minimum, and mean loads are based on 10-minute measurements or simulations using the computational model. The experimental results are based on 1,345 sets of 10-minute datasets of power production. The computational model calculated 10-minute real time turbine loads for every 2 m/s wind speed bin between the cut-in and cut-out speeds. At each wind speed, three different wind fields are simulated using TurbSim with the measured turbulence intensity. These calculated loads match experimental results. Blade loads increased with wind speed until the rated speed at which blades start to pitch was achieved. Beyond the rated speed, these loads decreased gradually.



(a)



(b)

Figure 10. Scatterplot for blade 1 flap and lead-lag bending loads

2.4.3 Result Correlation between the Analytical and Computational Models

Two extreme pitch fault cases are simulated using the computational model. They are: 1) blade 1 pitch stuck at 10 degree, and 2) blade 1 pitches at 1.5 degree and the other two blades pitch to feather. The analytical model uses the calculated rotor loads at the hub center as the input and the resulting front frame loads are compared against the computational model. A wind speed ramp from 3m/s to 25m/s over 225 seconds is used in the simulations of the pitch stuck case. Constant wind speed of 10m/s is used in the simulation of the pitch failure case. Figure 11(a) and Figure 11(b) show the time history of the front frame moments during these two pitch fault events calculated using the analytical and computational models. Results are normalized by comparing against the maximum pitching moment during the pitch stuck case. The agreement is excellent. As shown in Figure 11(a), during the first 25 seconds, wind speed is constant (3m/s) and the rotor imbalance is induced by the pitch stuck. Between 25 second and 100 second, the front frame loads increase with wind speed. After 100 second, the blade 2 and blade 3 start to pitch and the front frame loads decrease. The load reaches the minimal when the pitch angles of all blades equal 10 degree (rotor balance). Afterwards, the aerodynamic loads caused by high wind disturb the rotor balance, leading to the load increase at the front frame. As shown in Figure 11(b), at 25 second, blade 2 and blade 3 pitch quickly to the feathering position (around 90 degree) to stop the rotor. This results in a very large asymmetric rotor load due to the resulting pitch imbalance among the blades.

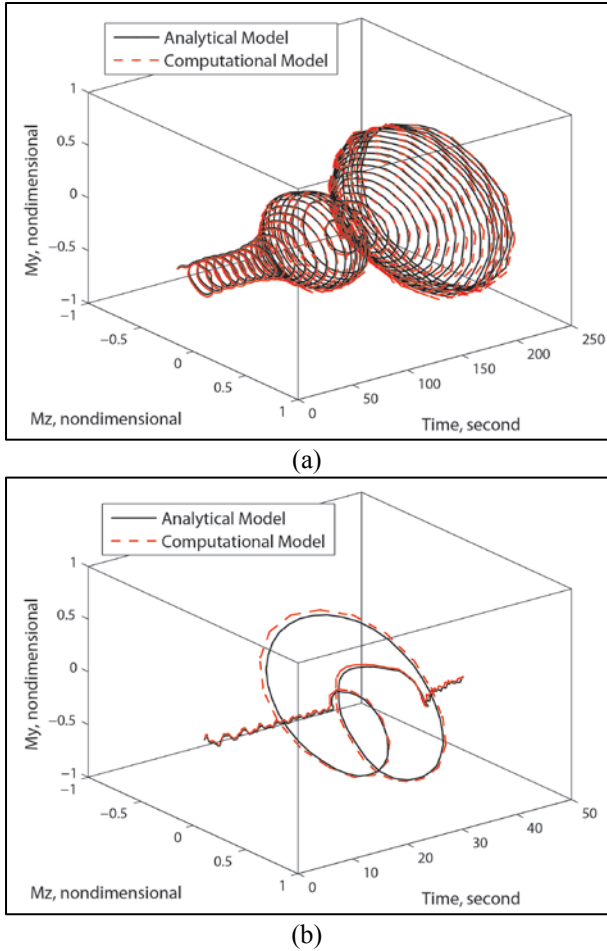


Figure 11. Dimensionless front frame bending moments during (a) pitch stuck and (b) pitch failure events

2.5 Evaluation of the Pure Torque Drivetrain

This section evaluates the Pure Torque drivetrain by studying main shaft bending loads during various field events, such as power production, normal stops with torque control, and emergency stop without torque control.

2.5.1 Main Shaft Loads during Power Production

Figure 12 compares the modeling and experimental results of main shaft pitching and yaw moments within the cut-in to cut-out wind speed range. The experimental results are binned for every 2 m/s wind speed from the cut-in to cut-out wind speeds and are based on 1,345 sets of 10-minute data. The statistic values of the experimental results are the maximum of the maximums, the mean of the means, and the minimum of the minimums of each wind speed bin.

Good agreement is evident among the computational model, analytical model, and experiment results. Small differences exist between the computational model and the other two approaches. Sensitivity study results indicate that the center of gravity locations of the planetary carrier may be different in the test turbine and analytical model compared to

the computational model. The different centers of gravity of the planetary carrier could be a potential source that results in higher pitching moment calculated by the computational model compared to experiments and analytical modeling results.

Within the entire wind speed range, the maximum shaft bending moment is less than 3% of the rated shaft torque, which is an order of magnitude less than the bending moment in the GRC three-point suspension drivetrain. The shaft loads do not change significantly with wind speed, which suggests a negligible influence of aerodynamics loads on the drivetrain. Additionally, the main shaft pitching moment of the Pure Torque drivetrain is mainly caused by the shaft weight, as shown in Eq. (12).

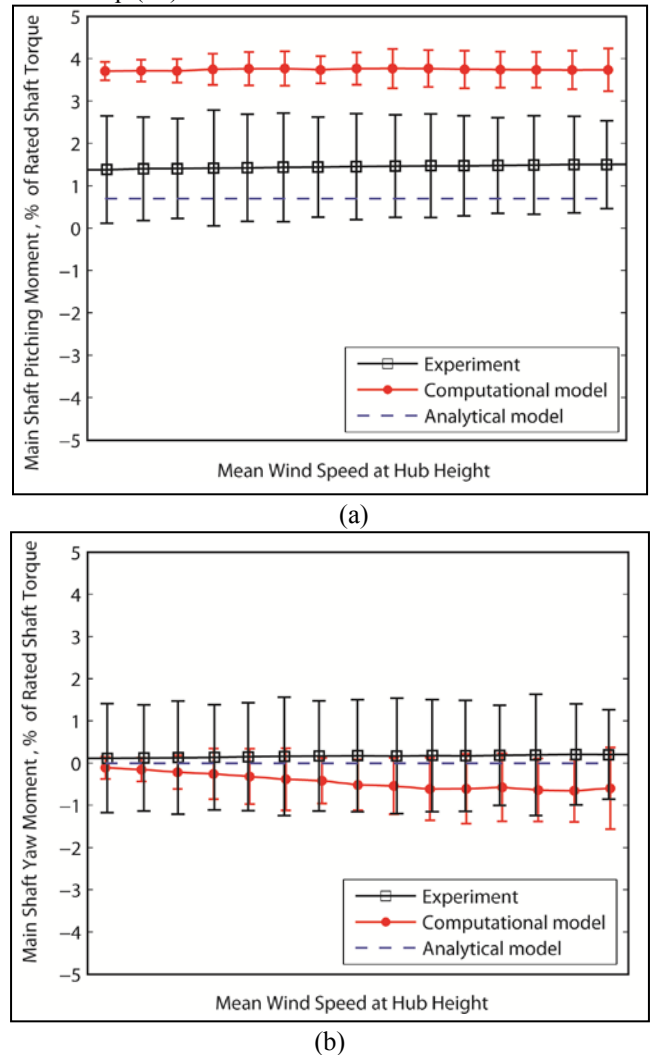
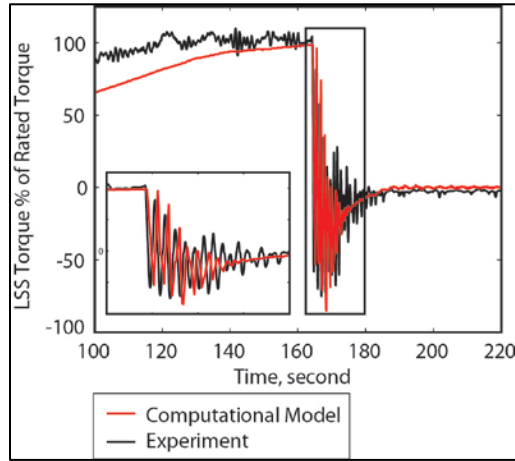


Figure 12. Main shaft (a) pitching and (b) yaw moments

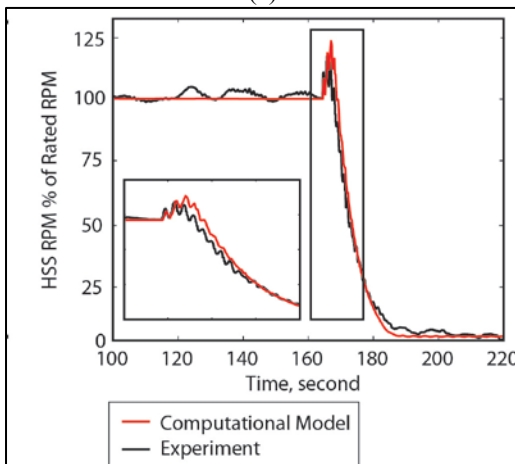
2.5.2 Main Shaft Loads during Extreme Transient Events

An emergency stop was manually performed during the test, and the turbine responses are compared between the modeling and experimental results in Figure 13. The results calculated by the computational model match the experimental

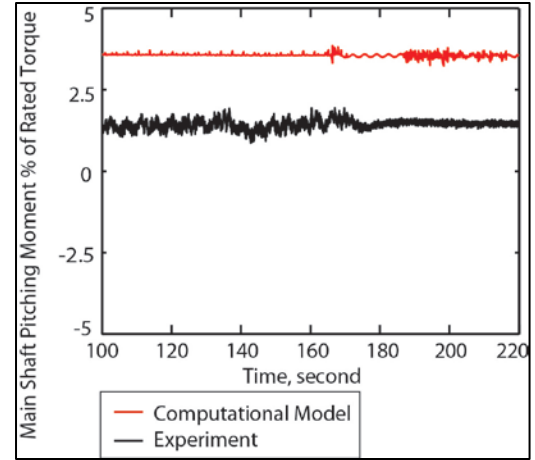
data well. The machine was operating at full power and rated speed and had an emergency stop at 157 s. At this instant, the shaft torque dropped immediately and became negative (80% of the rated torque). From 157 s to 180 s, the main shaft experienced torque reversals that lasted for 23 s. In the meantime, the high-speed RPM reached 120% of the rated speed at 157 s and reduced to zero within 23 s. Although the majority of the machine responses and loads changed rapidly during the emergency stop, the main shaft bending loads remained steady and the amplitudes were low as shown in Figure 13.



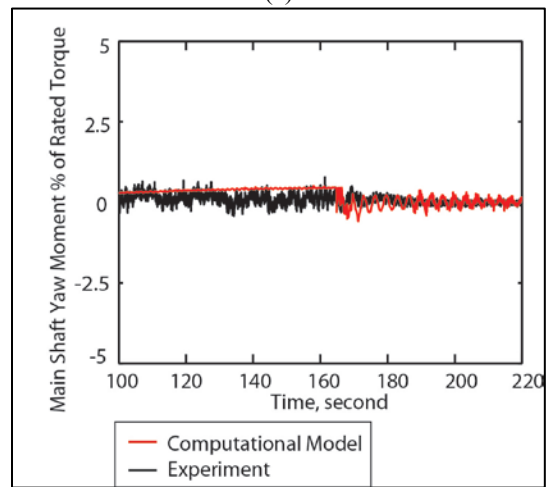
(a)



(b)



(c)



(d)

Figure 13. Turbine response: (a) rotor torque, (b) rotor speed, (c) main shaft pitching moment, and (d) main shaft yaw moment, during an emergency stop event

3 CONCLUSIONS

In Alstom's Pure Torque drivetrain, nearly all aerodynamic nontorque loads are diverted directly to the front frame instead of the drivetrain during various normal and extreme load cases. The front frame carries all the aerodynamic loads that have amplitudes comparable to the shaft torque. Gearbox misalignments and motions have low amplitudes during these events. Main shaft bending moments are mainly caused by the shaft's own weight. Their amplitudes are two orders of magnitude lower than the shaft torque.

A high-fidelity computational model was established in SAMCEF, and it was validated by experimental results for natural frequencies, turbine loads, and drivetrain loads. The flexibilities of the front frame, main shaft, and gearbox housing were important for accurately calculating the loads and deflections of the drivetrain and front frame. Having a detailed drivetrain module in the wind turbine dynamic model was

crucial to capturing the drivetrain dynamics and its interaction with the turbine response.

The reduced-order analytical model provided insight on the effects of nontorque rotor loads on the loads of various turbine components for the torque-only drivetrains. The methodology to derive the analytical model can be applied to other drivetrain configurations to quantify the influence of nontorque loads.

ACKNOWLEDGMENT

This work was financed by Alstom Wind under a Cooperative Research and Development Agreement with the National Renewable Energy Laboratory (CRD 10-400).

REFERENCES

- [1] Musial, W.; Butterfield, S.; and McNiff, B. (2007). "Improving wind turbine gearbox reliability", European Wind Energy Conference, Milan, Italy.
- [2] Link, H.; LaCava, W.; van Dam, J.; McNiff, B.; Sheng, S.; Wallen, R.; McDade, M.; Lambert, S.; Butterfield, S.; and Oyague, F. (2011) "Gearbox reliability collaborative project report: findings from phase 1 and phase 2", NREL Report No. TP-5000-51885, Golden, CO.
- [3] van Dam, J.; Riddle, T.; and Overly, E. (2007); "Torque measurements on GRC test turbine 1", NREL internal report.
- [4] Guo, Y. and Parker, R. G. (2010). "Dynamic modeling and analysis of a spur planetary gear involving tooth wedging", *European Journal of Mechanics A/Solid*, **29**, pp. 1022-1033.
- [5] Romax Technology, RomaxWind, <http://www.romaxtech.com/>
- [6] Guo, Y.; Keller, J.; and LaCava W. (2012); "Combined Effects of Gravity, Bending Moment, Bearing Clearance, and Input Torque on Wind Turbine Planetary gear Load Sharing", NREL Report No. CP-5000-55968, Golden, CO.
- [7] Guo, Y.; Keller, J.; and LaCava, W. (2014). "Wind turbine planetary load sharing of three-mount suspension drivetrains with non-torque loads", *Wind Energy*, DOI: 10.1002/we.1731.
- [8] Hidaka, T.; Terauchi, Y.; and Nagamura, K. (1976). "Dynamic behavior of planetary gear (1st report, load distribution in planetary gear)", *Bulletin of JSME*.
- [9] Bodas, A. and Kahraman, A. (2004) "Influence of carrier and gear manufacturing errors on the static load sharing behavior of planetary gear sets", *JSME International Journal. Series C. Mechanical Systems, Machine Elements and Manufacturing*, **47**(3), pp. 908-915.
- [10] Crowther, A.; Ramakrishnan, A.; Zaidi, N. A.; and Halse, C. (2011). "Sources of time-varying contact stress and misalignments in wind turbine planetary sets", *Wind Energy*, **14**, (5), pp. 637-651.
- [11] SAMCEF, "SAMCEF Wind Turbines V3.2", <http://www.lmsintl.com/simulation/wind-turbines>
- [12] Alstom Wind (2013). "ECO 100 wind turbine platform", <http://www.alstom.com/Global/Power/Resources/Documents/Brochures/eco-100-wind-turbine-platform.pdf>.
- [13] Garrad Hassan, "Bladed Multibody Dynamics V4.3 (Wind Turbine Design Software)", <http://www.g Garrad Hassan.com/en/GHBladed.php>.
- [14] Jonkman, J. "NWTC Design Codes", <http://wind.nrel.gov/designcodes/simulators/fast/>
- [15] Craig, R. R. (1985) "A review of time-domain and frequency-domain component mode synthesis method", *Journal of Modal Analysis*, **2**(2), pp. 59-72.
- [16] Bossanyi, E. A. (2004). "GH-Bladed User Manual", Issue 14, Bristol, UK: Garrad Hassan and Partners Limited.
- [17] Moriarty, P. J. (2005). "AeroDyn Theory Manual", NREL/TL-500-36881, National Renewable Energy Laboratory, Golden, CO.
- [18] Snel, H. and Schepers, J. G. (1995) "Joint Investigation of Dynamic Inflow Effects and Implementation of an Engineering Method", ECN Report ECNC-94-107.
- [19] Jonkman, B. and Buhl, M. L, Jr. (2006) "TurbSim User's Guide", NREL/TP-500-39797, Golden, CO.
- [20] IEC/FDIS (2005), "IEC-61400-1 Wind turbines - Part 1: design requirements", International standard.